

Label-free imaging of semiconducting and metallic carbon nanotubes in cells and mice using transient absorption microscopy

Ling Tong¹, Yuxiang Liu², Bridget D. Dolash³, Yookyung Jung⁴, Mikhail N. Slipchenko², Donald E. Bergstrom^{3,5} and Ji-Xin Cheng^{1,2,5*}

As interest in the potential biomedical applications of carbon nanotubes increases¹, there is a need for methods that can image nanotubes in live cells, tissues and animals. Although techniques such as Raman^{2–4}, photoacoustic⁵ and near-infrared photoluminescence imaging^{6–10} have been used to visualize nanotubes in biological environments, these techniques are limited because nanotubes provide only weak photoluminescence and low Raman scattering and it remains difficult to image both semiconducting and metallic nanotubes at the same time. Here, we show that transient absorption microscopy offers a label-free method to image both semiconducting and metallic single-walled carbon nanotubes *in vitro* and *in vivo*, in real time, with submicrometre resolution. By using appropriate near-infrared excitation wavelengths, we detect strong transient absorption signals with opposite phases from semiconducting and metallic nanotubes. Our method separates background signals generated by red blood cells and this allows us to follow the movement of both types of nanotubes inside cells and in the blood circulation and organs of mice without any significant damaging effects.

The biggest challenge associated with photoluminescence techniques is the low quantum yield (0.001–1.5%) of solution-suspended single-walled carbon nanotubes (SWNTs)^{11–13}. Although Ju *et al.*¹⁴ and Welsher *et al.*⁹ have shown that specific surface modification of nanotubes can enhance photoluminescence efficiency, the improvement is not applicable to nanotubes with other coatings. In practice, because separation is difficult, nanotube samples are often a mixture of semiconducting (S-SWNT) and metallic (M-SWNT) nanotubes. This poses an additional challenge to the photoluminescence technique, because only S-SWNTs exhibit photoluminescence¹¹. Recently a four-wave mixing signal has been applied to image individual nanotubes, but this is only sensitive to M-SWNTs¹⁵.

Transient absorption microscopy is an emerging tool for label-free imaging¹⁶. In this method the pump field perturbs the electronic states of the material and the probe field responds to the changed electronic states, resulting in a transiently enhanced or reduced absorption of the probe field. The transient absorption signal has been used for mapping pigments and haemoglobin¹⁶, nanoparticles^{17–19}, nanotubes²⁰ and non-fluorescent chromophores²¹, but has not been used to image nanostructures in real time within live cells and tissues. *In vivo* transient absorption imaging is particularly difficult because of the strong background signal generated from the haemoglobin absorption-induced photothermal lens effect. In this

work, we overcome this background by phase separation of the transient absorption signals from the nanotubes and the photothermal lens signals from blood. By using appropriate near-infrared excitation wavelengths, we report strong transient absorption signals with opposite phases from S- and M-SWNTs, as well as the application of the signals to visualize both types of nanotubes in live cells, tissues and live animals with submicrometre resolution and negligible photodamage.

Transient absorption signals from pure electric-arc S-SWNTs and M-SWNTs were obtained on a laser-scanning transient absorption microscope (Supplementary Fig. S1)²⁰. With the pump beam at 707 nm (near $E_{11}^M = 600–800$ nm) and the probe beam at 885 nm (near $E_{22}^S = 850–1,100$ nm), S-SWNTs (Fig. 1a, left) and M-SWNTs (Fig. 1a, middle) displayed positive (Fig. 1b, left) and negative (Fig. 1b, middle) signals in the in-phase channel, respectively, whereas little signal was detected in the quadrature channel (Supplementary Fig. S2), corresponding to an in-phase and anti-phase modulation of the probe beam for S-SWNTs and M-SWNTs, respectively. The metallic properties were confirmed by measuring the Raman spectra²² with the microRaman capability on the same platform²³ (Fig. 1c, left and middle).

To test whether this method can map the metallicity of nanotubes in a biological environment, we prepared nanotubes with different surface coatings. We dispersed electric-arc nanotubes in oligodeoxyribonucleotides (GT)₁₅ solution by sonication²⁴. An atomic force microscopy (AFM) image (Supplementary Fig. S3) showed that the DNA-wrapped nanotubes were well dispersed with an average length of 244 ± 135 nm. A series of peaks in the extinction spectrum revealed the interband transitions, with the peaks around 850–1,100 nm and 600–800 nm assigned to E_{22}^S and E_{11}^M , respectively (Fig. 1a, right). Using the same imaging conditions, two populations of signals with positive or negative contrast were detected in the in-phase channel (Fig. 1b, right), whereas little signal showed up in the quadrature channel (Supplementary Fig. S2). MicroRaman spectroscopy²³ confirmed the positive and negative signals were from S-SWNTs and M-SWNTs²², respectively (Fig. 1c, right). To test the sensitivity and resolution of the method, we imaged aligned SWNTs grown on special cut quartz substrate. Individual S-SWNTs and M-SWNTs could be clearly visualized with opposite phases and submicrometre resolution (Supplementary Fig. S4). Our method is applicable to nanotubes with various surface coatings including pluronic polymer F127, surfactant sodium cholate and surfactant sodium dodecyl sulphate (Supplementary Fig. S5).

¹Department of Chemistry, Purdue University, West Lafayette, Indiana 47907, USA, ²Weldon School of Biomedical Engineering, Purdue University, West Lafayette, Indiana 47907, USA, ³Department of Medical Chemistry and Molecular Pharmacology, Purdue University, West Lafayette, Indiana 47907, USA, ⁴Department of Physics, Purdue University, West Lafayette, Indiana 47907, USA, ⁵Birk Nanotechnology Center, Purdue University, West Lafayette, Indiana 47907, USA. *e-mail: jcheng@purdue.edu

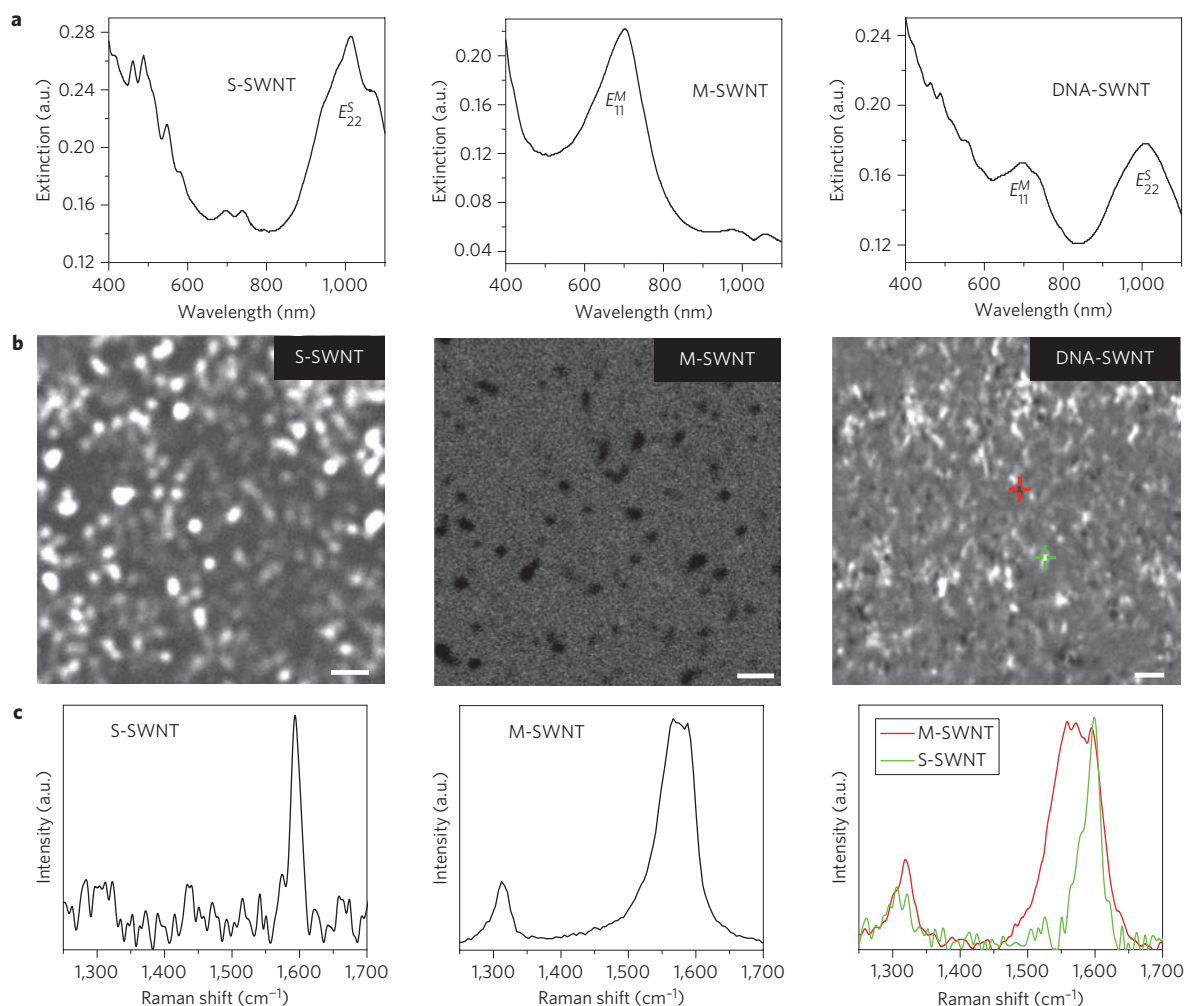


Figure 1 | Semiconducting and metallic nanotubes exhibit strong transient absorption signals with opposite phases. **a**, Extinction spectra of pure S-SWNT (left), pure M-SWNT (middle) and DNA-wrapped nanotubes (DNA-SWNT) (right) solutions. E_{11}^M , first optical transition of M-SWNTs; E_{22}^S , second optical transition of S-SWNTs. **b**, Transient absorption images of pure S-SWNTs (left), pure M-SWNTs (middle) and DNA-SWNTs (right) in the in-phase channel. S-SWNTs and M-SWNTs showed positive and negative contrast, respectively. Scale bars, 2 μm . For all transient absorption images, pump and probe beams were at 707 nm and 885 nm, respectively. The laser power after the objective was 0.7 mW for the pump beam and 1.3 mW for the probe beam. **c**, Raman spectra from pure S-SWNTs (left), pure M-SWNTs (middle) and DNA-SWNTs (right).

To clarify the origin of the intense signals, we first tuned the pump/probe energy difference in ($2,600 \text{ cm}^{-1}$) and out of ($2,850 \text{ cm}^{-1}$) resonance with the G' band. The signals were found to be at the same level, indicating that stimulated Raman scattering by the G' band was negligible compared to the transient absorption signal (Supplementary Fig. S6). Transient absorption is a complex process that could be contributed by several mechanisms including ground-state depletion, stimulated emission, excited-state absorption and multiphoton absorption¹⁶. When the pump beam was fixed at 707 nm and the probe beam scanned from 810 nm to 955 nm, the signals remained positive for S-SWNTs and negative for M-SWNTs (Supplementary Fig. S7a). The anti-phase signal from M-SWNTs could be explained by photo-induced broadening of the transition width after absorption of the 707 nm pump beam by the free electrons in the M-SWNTs²⁵, and subsequent enhanced transient absorption (negative signal) of the probe beam (885 nm) off resonance with E_{11}^M (Supplementary Fig. S7b)²⁰. For S-SWNTs, the signal increased as the probe wavelength increased and approached the gap energy of E_{22}^S , indicating that stimulated emission might contribute to the positive signal²⁰.

We notice that nanotubes have different chiralities, with corresponding sharp absorption and emission peaks. However, we did

not observe any significant change in the contrast when we tuned the wavelength of the probe beam (Supplementary Fig. S8), suggesting that the detected signal might not arise from the chirality peak absorption signals, but from the baseline absorption. We further imaged the same nanotube sample using AFM and transient absorption microscopy. As shown in Fig. 2, 21 of a total of 25 S-SWNTs (84%) and 15 of a total of 17 M-SWNTs (88%) seen in the AFM image were apparent in the transient absorption image, respectively. These results demonstrate that transient absorption microscopy can map both S-SWNTs and M-SWNTs in a chirality-insensitive manner.

We applied the transient absorption signal to monitor the cellular uptake and intracellular trafficking of DNA-wrapped nanotubes in live Chinese hamster ovary (CHO) cells (Supplementary Fig. S9). The intense transient absorption signals allowed us to monitor the trafficking of nanotubes in a single cell without photobleaching and photodamage. Several types of intracellular trafficking motions were observed, including active transport, fusion and return to the cell surface (Fig. 3, Supplementary Videos S1, S2). Exemplary trajectories were analysed by the single particle tracking method for both S-SWNTs and M-SWNTs (Supplementary Figs S10, S11). Quantitative analysis of the trajectories (Supplementary Fig. S12) showed that once internalized

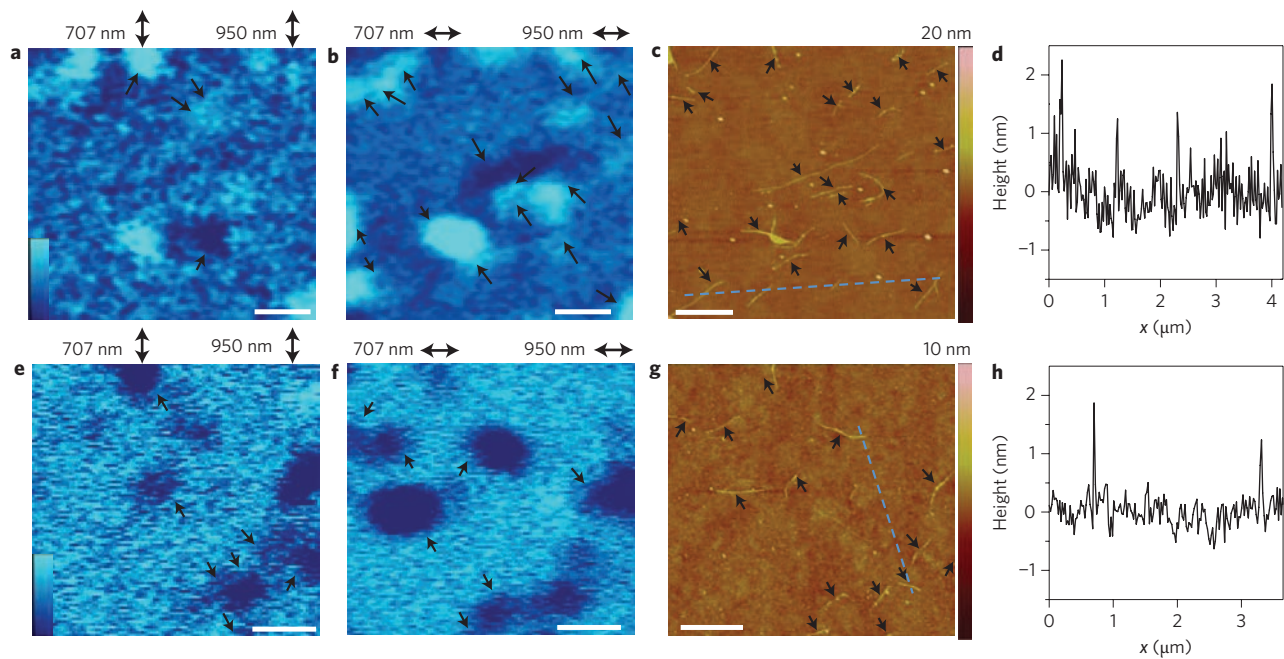


Figure 2 | Comparison of transient absorption and AFM images of the same nanotube sample show that transient absorption microscopy can detect M-SWNTs and S-SWNTs in a chirality-insensitive manner. a–c, Transient absorption image (**a,b**) and AFM image (**c**) of pure S-SWNTs in the same area. **e–g,** Transient absorption image (**e,f**) and AFM image (**g**) of pure M-SWNTs in the same area. The pump and probe polarization directions are vertical in **a** and **e** and horizontal in **b** and **f**, as indicated by two-headed arrows above the transient absorption images. Nanotubes that are detected by transient absorption images are labelled with arrows on both the transient absorption and AFM images. In total, 21 of 25 S-SWNTs (84%) and 15 of 17 M-SWNTs (88%) seen in the AFM image were shown in the transient absorption image, respectively. Scale bars, 1 μm . Laser power post-objective was 0.7 mW for the pump beam and 1.3 mW for the probe beam. **d,h,** Height analyses along the blue dotted lines in **c** and **g**, respectively, show individual nanotubes, not bundles.

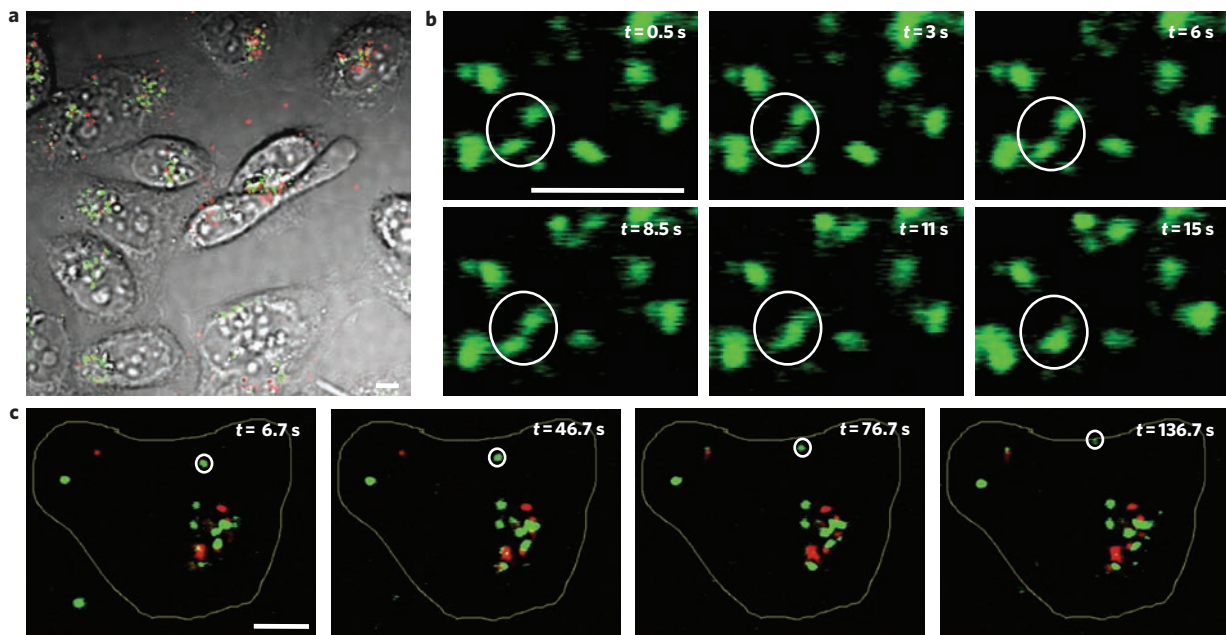


Figure 3 | Cellular uptake and intracellular trafficking of DNA-SWNTs monitored in real time by transient absorption microscopy. a, Transient absorption image of DNA-SWNTs internalized by CHO cells after 24 h incubation. **b,** Time-lapse images showing the fusion process for two nanotubes (indicated by white circle). **c,** Time-lapse images showing the transport of a nanotube (indicated by white circle) back to the cell surface. The yellow line outlines the cell. Grey, transmission of cells; green, S-SWNTs; red, M-SWNTs. Scale bars, 5 μm . Pump, 707 nm; probe, 885 nm. The laser power post-objective was 1 mW for the pump beam and 1.6 mW for the probe beam.

without forming big aggregates, the endosomes containing the DNA-wrapped electric-arc S-SWNTs and M-SWNTs displayed similar intracellular trafficking activities.

For *in vivo* applications we administrated F127-wrapped nanotubes (Supplementary Fig. S13) to Balb/c mice by tail vein injection and monitored the circulation of individual nanotubes in the blood

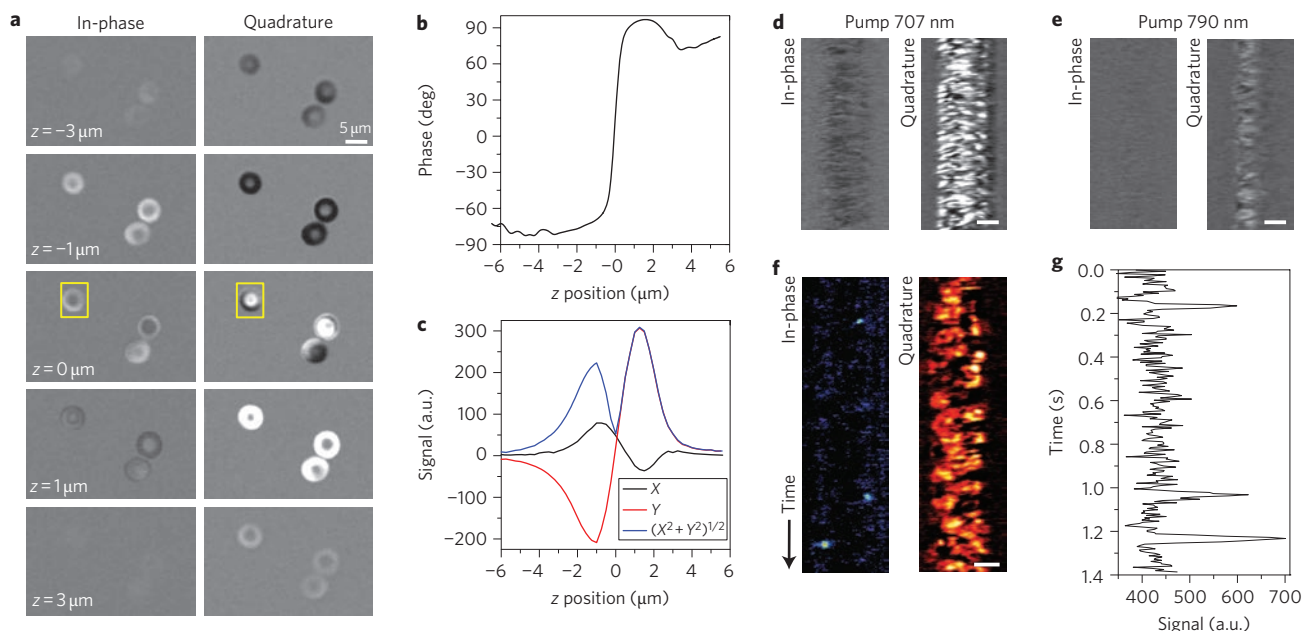


Figure 4 | Imaging of RBCs and F127-wrapped SWNTs (F127-SWNTs) circulating in the blood vessels of a mouse earlobe. **a**, Thermal lens signals from isolated RBCs at different z -positions with $z = 0 \mu\text{m}$ as the middle plane of a RBC. Pump, 707 nm; probe, 885 nm. **b**, Phase of thermal lens signals from a RBC as a function of focus position. **c**, In-phase channel signal (X), quadrature channel signal (Y) and amplitude of the thermal lens signal ($R = (X^2 + Y^2)^{1/2}$) from a RBC as a function of focus position. **d,e**, Intravital thermal lens imaging of RBCs in the blood vessel inside the earlobe of a mouse injected with pure saline when the pump beam is at 707 nm (**d**) and 790 nm (**e**). The probe beam was fixed at 885 nm for both cases. Images were taken by line scanning (x - t scanning, 132 pixels per line). **f**, Intravital imaging of F127-SWNTs in the blood vessel inside the earlobe of a mouse by line scanning (x - t scanning, 105 pixels per line). In-phase channel: transient absorption signals from F127-SWNTs. Quadrature channel: thermal lens signals from RBCs. Pump and probe beams were at 790 nm and 885 nm, respectively. Laser power post-objective was 16 mW for both beams. Scale bars (**d-f**), 3 μm . **g**, Intensity profile showing three peaks corresponding to the three dots in **f**.

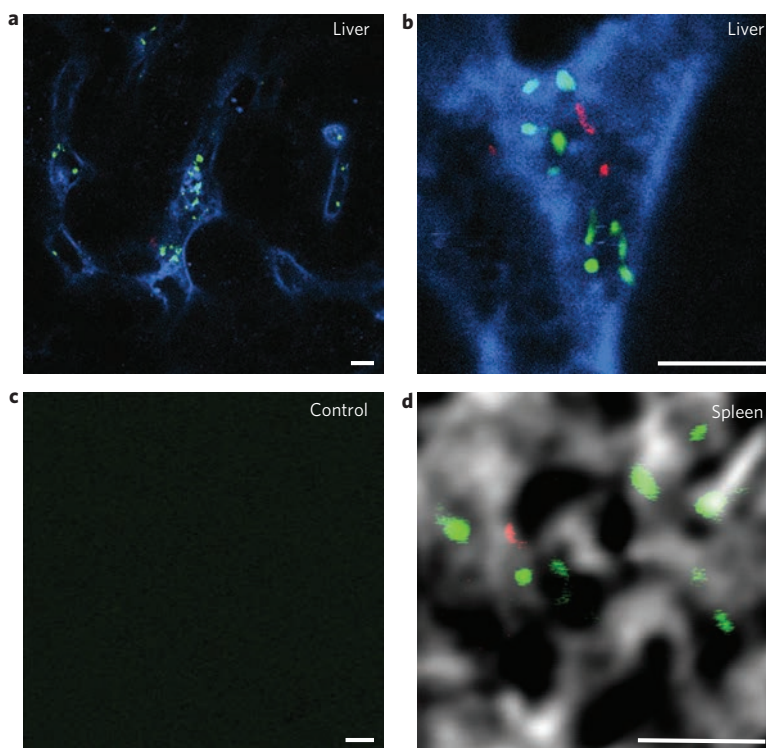


Figure 5 | F127-SWNTs in different organs of treated mice are visualized by transient absorption microscopy at the cellular level. **a**, Image of F127-SWNTs in liver tissue with Kupffer cells labelled with ED-1 antibody. Green, S-SWNTs; red, M-SWNTs; blue, two-photon fluorescent signal from antibody. **b**, A zoom-in image of nanotubes in a Kupffer cell in the liver. **c**, Image of normal liver tissue without nanotubes. **d**, Image of nanotubes in spleen tissue. Grey, transmission of tissue. Scale bars, 5 μm . Pump, 707 nm; probe, 885 nm. Laser power post-objective was 1.0 mW for the pump beam and 1.6 mW for the probe beam.

vessel inside the earlobe. To reduce the concomitant photothermal lens signals from red blood cells (RBCs)²⁶, we first examined the signals from single isolated RBCs using our set-up. The signal was dependent on the focus position in the z -direction (Fig. 4a–c), with a phase change of $\sim 180^\circ$ and minimum amplitude at the middle plane of the RBC ($z = 0 \mu\text{m}$). These characteristics are consistent with the features of the thermal lens effect²⁷. The signal in the quadrature channel was found to be two times stronger than that in the in-phase channel, partly because of the megahertz modulation. We further minimized the thermal lens signal from RBCs in the in-phase channel by changing the wavelength of the pump beam from 707 nm to 790 nm, where the absorption of haemoglobin was weaker. As shown in Fig. 4d,e, the thermal lens signals in both channels were reduced when the pump beam was tuned to 790 nm, with a negligible contrast in the in-phase channel image. Because the transient absorption signals from nanotubes appeared only in the in-phase channel (Supplementary Fig. S2), they were well separated from the thermal lens signals in the quadrature channel. This phase separation enabled us to visualize nanotubes and RBCs simultaneously (Supplementary Video S3). By line-scanning across the blood vessel (Fig. 4f,g), we were able to detect nanotubes with a high signal-to-noise ratio in the in-phase channel and RBCs in the quadrature channel. We observed no photodamage to tissues or photothermal degradation of nanotubes during scanning.

With the transient absorption signals, we further mapped the distribution of F127-wrapped nanotubes in extracted organs. Nanotubes were visualized in liver and spleen (Fig. 5). With very low laser power after the objective (1 mW for the pump beam, 1.6 mW for the probe beam), no autofluorescence or photothermal signals from the tissues were detected (Fig. 5c). Nanotubes were accumulated inside Kupffer cells, as confirmed by immunofluorescence labelling. Both S-SWNTs and M-SWNTs were detected and labelled, with green and red representing their opposite phases. We were also able to image nanotubes in bulk tissue using the backward detection channel (Supplementary Fig. S14), providing the modality for further *in vivo* study.

In conclusion, by coupling transient absorption spectroscopy^{25,28} with scanning microscopy, we have demonstrated a new approach for high-speed visualization of single-walled carbon nanotubes. Because of the different bandgap energies, the S- and M-SWNTs exhibit transient absorption signals with opposite phases under the current pump/probe conditions. Our method is applicable to carbon nanotubes with different coatings and allows time-lapse visualization of S-SWNTs and M-SWNTs in live cells and animals. Transient absorption microscopy provides a novel platform with which to study nanotubes and other nanostructures with sub-micrometre resolution, individual nanotube sensitivity, real-time imaging speed and spectral information. This technique offers a way to study nano–bio interactions and the cytotoxicity of nanotubes.

Methods

Transient absorption microscopy. A schematic of our transient absorption microscope is shown in Supplementary Fig. S1. Two 5 ps lasers (Tsunami Spectra-Physics) assigned as pump and probe beams were synchronized and collinearly combined into an inverted confocal microscope (FV300/IX71, Olympus America). The pump laser intensity was modulated by a Pockels cell (360–80, Con-optics) at a frequency of 1.13 MHz. The two laser beams were focused onto the sample by a $\times 60$ (NA = 1.2) or $\times 40$ (NA = 0.8) water objective (Olympus). The forward signal was collected by another $\times 60$ water objective or an air condenser (NA = 0.55), detected by a large-area photodiode (818-BB-40, Newport) after passing a bandpass filter of 850/90 nm or a 900 nm long-pass filter to block the pump beam. A lock-in amplifier (SR844, Stanford Research Systems) was used to pick up the transient absorption signals with a function generator modulated at a modulation frequency of 1.13 MHz. Assuming the modulated component of an input signal is $I_{\text{in}}\sin(\Omega t + \varphi_{\text{in}})$, the output signals in the two channels of the lock-in amplifier are proportional to $I_{\text{in}}\cos(\varphi_{\text{in}} - \varphi_{\text{R}})$ and $I_{\text{in}}\sin(\varphi_{\text{in}} - \varphi_{\text{R}})$, where I_{in} , Ω , φ_{in} and φ_{R} are the amplitude of the modulated signal, the modulation frequency, the phase of the input signal, and the reference phase of the lock-in amplifier, respectively. Before measuring the samples,

we calibrated the reference phase by sending the modulated pump field, $I_{\text{pump}}\sin(\Omega t + \varphi_{\text{pump}})$, to the photodiode. In this case, the output signals of the lock-in amplifier were proportional to $I_{\text{pump}}\cos(\varphi_{\text{pump}} - \varphi_{\text{R}})$ and $I_{\text{pump}}\sin(\varphi_{\text{pump}} - \varphi_{\text{R}})$, where φ_{pump} is the phase of the modulated pump field. By setting $\varphi_{\text{R}} = \varphi_{\text{pump}}$, the output signal from the cosine channel and the sine channel became maximum and zero, respectively. We defined the cosine channel as the in-phase channel and the sine channel as the quadrature channel. When a modulated probe signal, $I_{\text{probe}}\sin(\Omega t + \varphi_{\text{probe}})$, was detected by the lock-in amplifier, the in-phase channel and quadrature-channel output signals were described as $X = I_{\text{probe}}\cos(\varphi_{\text{probe}} - \varphi_{\text{pump}})$ and $Y = I_{\text{probe}}\sin(\varphi_{\text{probe}} - \varphi_{\text{pump}})$, respectively. The phase of the probe relative to the pump was defined as $\varphi_{\text{probe}} - \varphi_{\text{pump}} = \tan^{-1}(Y/X)$. The time constant, filter slope and sensitivity of the lock-in amplifier were set as 100 μs , 6 dB and 100 μV for SWNT imaging. The output channel of the lock-in amplifier was positively biased to avoid the feeding of a negative signal into an analog-to-digital converter, which had a range from 0 to 5 V. Images were acquired with 200 μs per pixel dwell time for SWNTs dried on coverglass or in tissues and 50 μs per pixel for moving SWNTs in cells or blood vessels. Confocal Raman signals were recorded using a spectrometer (Shamrock SR-303i-A, Andor Technology) mounted to the side port of the microscope²³.

Preparation and characterization of SWNTs. DNA wrapping of electric-arc SWNTs (CarboLex) followed the protocol developed by the Bergstrom group²⁴. DNA-wrapped SWNTs and F127-wrapped SWNTs were characterized by a UV-vis-NIR spectrophotometer, AFM, Raman spectroscopy and transient absorption microscopy. Extinction spectra were measured from diluted SWNT solutions with a UV-vis-NIR spectrophotometer (DU530, Beckman) in the range 400–1,100 nm. AFM images of SWNTs dried on a mica substrate were taken on a scanning probe microscope (Dimensions 3100, Veeco) in tapping mode using silicon probes with a nominal resonance frequency of 300 kHz. For transient absorption imaging and microRaman spectroscopy, SWNTs were dried on a clean coverslip. The laser power after the objective for pump and probe beams was 0.7 mW and 1.3 mW, respectively.

Cell, tissue and intravital imaging. For cellular imaging, CHO cells were treated with DNA-wrapped SWNTs and incubated at 37 °C for different periods of time. Intracellular trafficking modes were analysed using a single particle tracking method as described previously²⁹. A total of 15 S-SWNTs and 10 M-SWNTs in five cells were tracked. For tissue imaging, mice were killed 24 h after *i.v.* injection of SWNTs. Organs including liver, spleen and kidney were explanted and fixed in 4% formalin solution to preserve the tissue architecture. Organs were cut into 100 μm slices. For intravital imaging of SWNTs in flowing blood, 100 μl of F127-wrapped SWNT solution (0.25 mg ml⁻¹) was administered to BALB/c mice by tail vein injection. Details are provided in the Supplementary Information.

Received 2 September 2011; accepted 31 October 2011;
published online 4 December 2011

References

- Liu, Z., Tabakman, S., Welsher, K. & Dai, H. Carbon nanotubes in biology and medicine: *in vitro* and *in vivo* detection, imaging and drug delivery. *Nano Res.* **2**, 85–120 (2009).
- Heller, D., Baik, S., Eurell, T. & Strano, M. Single-walled carbon nanotube spectroscopy in live cells: towards long-term labels and optical sensors. *Adv. Mater.* **17**, 2793–2799 (2005).
- Liu, Z. *et al.* Multiplexed multicolor Raman imaging of live cells with isotopically modified single walled carbon nanotubes. *J. Am. Chem. Soc.* **130**, 13540–13541 (2008).
- Zavaleta, C. *et al.* Noninvasive Raman spectroscopy in living mice for evaluation of tumor targeting with carbon nanotubes. *Nano Lett.* **8**, 2800–2805 (2008).
- De La Zerda, A. *et al.* Carbon nanotubes as photoacoustic molecular imaging agents in living mice. *Nature Nanotech.* **3**, 557–562 (2008).
- Cherukuri, P., Bachilo, S. M., Litovsky, S. H. & Weisman, R. B. Near-infrared fluorescence microscopy of single-walled carbon nanotubes in phagocytic cells. *J. Am. Chem. Soc.* **126**, 15638–15639 (2004).
- Jin, H., Heller, D. A. & Strano, M. S. Single-particle tracking of endocytosis and exocytosis of single-walled carbon nanotubes in NIH-3T3 cells. *Nano Lett.* **8**, 1577–1585 (2008).
- Leeuw, T. K. *et al.* Single-walled carbon nanotubes in the intact organism: near-IR imaging and biocompatibility studies in drosophila. *Nano Lett.* **7**, 2650–2654 (2007).
- Welsher, K. *et al.* A route to brightly fluorescent carbon nanotubes for near-infrared imaging in mice. *Nature Nanotech.* **4**, 773–780 (2009).
- Welsher, K., Sherlock, S. P. & Dai, H. Deep-tissue anatomical imaging of mice using carbon nanotube fluorophores in the second near-infrared window. *Proc. Natl Acad. Sci. USA* **108**, 8943–8948 (2011).
- O'Connell, M. J. *et al.* Band gap fluorescence from individual single-walled carbon nanotubes. *Science* **297**, 593–596 (2002).
- Nish, A., Hwang, J.-Y., Doig, J. & Nicholas, R. J. Highly selective dispersion of single-walled carbon nanotubes using aromatic polymers. *Nature Nanotech.* **2**, 640–646 (2007).

13. Crochet, J., Clemens, M. & Hertel, T. Quantum yield heterogeneities of aqueous single-wall carbon nanotube suspensions. *J. Am. Chem. Soc.* **129**, 8058–8059 (2007).
14. Ju, S.-Y., Kopcha, W. P. & Papadimitrakopoulos, F. Brightly fluorescent single-walled carbon nanotubes via an oxygen-excluding surfactant organization. *Science* **323**, 1319–1323 (2009).
15. Kim, H., Sheps, T., Collins, P. G. & Potma, E. O. Nonlinear optical imaging of individual carbon nanotubes with four-wave-mixing microscopy. *Nano Lett.* **9**, 2991–2995 (2009).
16. Ye, T., Fu, D. & Warren, W. S. Nonlinear absorption microscopy. *Photochem. Photobiol.* **85**, 631–645 (2009).
17. Van Dijk, M. A., Lippitz, M. & Orrit, M. Detection of acoustic oscillations of single gold nanospheres by time-resolved interferometry. *Phys. Rev. Lett.* **95**, 267406 (2005).
18. Muskens, O. L., Del Fatti, N. & Valle, F. Femtosecond response of a single metal nanoparticle. *Nano Lett.* **6**, 552–556 (2006).
19. Hartland, G. V. Ultrafast studies of single semiconductor and metal nanostructures through transient absorption microscopy. *Chem. Sci.* **1**, 303–309 (2010).
20. Jung, Y. *et al.* Fast detection of the metallic state of individual single-walled carbon nanotubes using a transient-absorption optical microscope. *Phys. Rev. Lett.* **105**, 217401 (2010).
21. Min, W. *et al.* Imaging chromophores with undetectable fluorescence by stimulated emission microscopy. *Nature* **461**, 1105–1109 (2009).
22. Jorio, A. *et al.* Characterizing carbon nanotube samples with resonance Raman scattering. *New J. Phys.* **5**, 139 (2003).
23. Slipchenko, M. N., Le, T. T., Chen, H. & Cheng, J.-X. High-speed vibrational imaging and spectral analysis of lipid bodies by compound Raman microscopy. *J. Phys. Chem. B* **113**, 7681–7686 (2009).
24. Roy, L., Bridget, D., Donald, B. & Ronald, R. Oligodeoxyribonucleotide association with single-walled carbon nanotubes studied by SPM. *Small* **3**, 1912–1920 (2007).
25. Ellingson, R. J. *et al.* Ultrafast photoresponse of metallic and semiconducting single-wall carbon nanotubes. *Phys. Rev. B* **71**, 115444 (2005).
26. Lu, S., Min, W., Chong, S., Holtom, G. R. & Xie, X. S. Label-free imaging of heme proteins with two-photon excited photothermal lens microscopy. *Appl. Phys. Lett.* **96**, 113701 (2010).
27. Uchiyama, K., Hibara, A., Kimura, H., Sawada, T. & Kitamori, T. Thermal lens microscope. *Jpn J. Appl. Phys.* **39**, 5316–5322 (2000).
28. Laurent, J. S. *et al.* Ultrafast carrier dynamics in single-wall carbon nanotubes. *Phys. Rev. Lett.* **90**, 057404 (2003).
29. Tong, L., Lu, Y., Lee, R. J. & Cheng, J.-X. Imaging receptor-mediated endocytosis with a polymeric nanoparticle-based coherent anti-Stokes Raman scattering probe. *J. Phys. Chem. B* **111**, 9980–9985 (2007).

Acknowledgements

The authors thank Z. Zhong for providing the aligned SWNT samples, J.H. Choi for measuring the photoluminescence emission spectrum from SWNT samples, and A. Ivanisevic for assisting with AFM measurements. This work was supported by the National Science Foundation (grant no. 0828832 to J.X.C.), the Bilsland Fellowship (L.T.) and the Walther Cancer Institute and Lilly Foundation (D.E.B.).

Author contributions

L.T. and J.X.C. conceived and designed the experiments. L.T. and Y.L. performed the experiments. L.T. and Y.L. analysed the data. B.D.D., Y.J., M.N.S. and D.E.B. contributed materials and analysis tools. L.T. and J.X.C. co-wrote the paper. All authors discussed the results and commented on the manuscript.

Additional information

The authors declare no competing financial interests. Supplementary information accompanies this paper at www.nature.com/naturenanotechnology. Reprints and permission information is available online at <http://www.nature.com/reprints>. Correspondence and requests for materials should be addressed to J.X.C.